

# Cable-Driven Haptic Interface With Movable Bases Achieving Maximum Workspace and Isotropic Force Exertion

Jinhyuk Yoon<sup>ID</sup>, Donghyeon Lee<sup>ID</sup>, Junyong Bang, Hyung Gon Shin<sup>ID</sup>, Wan Kyun Chung<sup>ID</sup>, *Fellow, IEEE*, Seungmoon Choi<sup>ID</sup>, *Senior Member, IEEE*, and Keehoon Kim<sup>ID</sup>, *Member, IEEE*

**Abstract**—Haptic interactions play an essential role in education to enhance learning efficiency; however, haptic information for virtual educational content remains lacking. This article proposes a planar cable-driven haptic interface with movable bases that can display isotropic force feedback with maximum workspace extension on a commercial screen display. A generalized kinematic and static analysis of the cable-driven mechanism is derived by considering movable pulleys. Based on the analyses, a system including movable bases is designed and controlled to maximize the workspace subject to isotropic force exertion for the target screen area. The proposed system is evaluated experimentally as a haptic interface represented by the workspace, isotropic force-feedback range, bandwidth, Z-width, and user experiment. The results indicate that the proposed system can maximize workspace to the target rectangular area and exert isotropic force up to 94.0% of the theoretical computed one within the workspace.

**Index Terms**—Adaptive mechanism, cable-driven interface, force feedback, haptic device, kinesthetic device.

## I. INTRODUCTION

CORONAVIRUS-2019 accelerated changes in the educational environment from face-to-face to virtual education. Virtual content can provide a rich learning experience thanks

Manuscript received 29 October 2022; revised 18 March 2023 and 23 May 2023; accepted 8 June 2023. Date of publication 19 June 2023; date of current version 19 September 2023. This work was supported in part by the Support Program for Reinforcement of Science Culture Exhibition Service under Grant NRF-2020X1A3A1095082 from the NRF in the Republic of Korea and in part by the Technology Development Program under Grant No. S3177366 funded by the Ministry of SMEs and Startups (MSS, Korea). This paper was recommended for publication by Associate Editor Matteo Bianchi and Editor-in-Chief Marcia K O’Malley upon evaluation of the reviewers’ comments. (*Corresponding author: Keehoon Kim.*)

This work involved human subjects or animals in its research. The author(s) confirm(s) that all human/animal subject research procedures and protocols are exempt from review board approval.

Jinhyuk Yoon, Donghyeon Lee, Junyong Bang, Hyung Gon Shin, Wan Kyun Chung, and Keehoon Kim are with the Department of Mechanical Engineering, Pohang University of Science and Technology, Pohang 37673, South Korea (e-mail: jinhyukyoon@postech.ac.kr; sansoveria@postech.ac.kr; bangjy0727@postech.ac.kr; tlsgudrh@postech.ac.kr; wkchung@postech.ac.kr; khk@postech.ac.kr).

Seungmoon Choi is with the Department of Computer Science and Engineering, Pohang University of Science and Technology, Pohang 37673, South Korea (e-mail: choism@postech.ac.kr).

This article has supplementary downloadable material available at <https://doi.org/10.1109/TOH.2023.3286353>, provided by the authors.

Digital Object Identifier 10.1109/TOH.2023.3286353

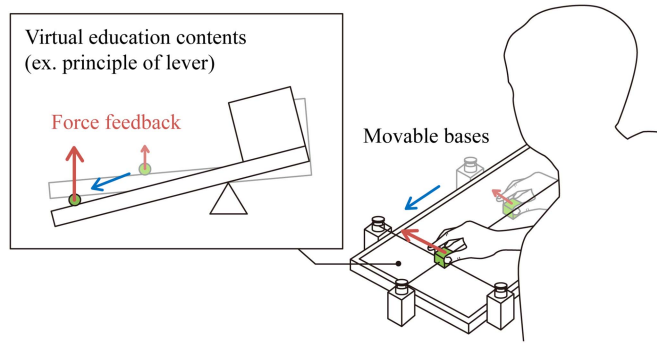


Fig. 1. An example of application scenario featuring the proposed two-degree-of-freedom (2-DoF) planar cable-driven haptic interface with movable bases.

to its variability. However, most of the virtual content focuses on visual information and does not involve haptic engagement, which can further improve learning efficiency in various disciplines [1], [2], [3], [4], [5]. In particular, haptic interaction with force and kinesthetic feedback helped elementary students to learn physics concepts with better retention, inference, and comprehension [1], [2]. To provide haptic interaction on virtual content, it is necessary to build a haptic interface.

A concept for an educational haptic interface can be a planar haptic device that can be installed on smart devices and commercial screen displays, such as televisions, tablet, and personal computers. This type of haptic interface may facilitate haptic interaction in existing educational content and settings (Fig. 2). However, several technical requirements need to be matched to facilitate the implementation of this concept: the workspace of the haptic interface should cover the entire rectangular screen to ensure the absence of blind spots, moreover, the haptic mechanism should display sufficient isotropic forces over the entire workspace.

Among various actuation mechanisms for haptic interfaces available in literature [6], for the device presented in this study we selected a cable-driven mechanism owing to its low-inertial, low-backlash, and high-load-to-weight-ratio characteristics. The mechanism also has a powerful advantage in the fact that thin cables minimize visual interference while users can observe virtual content on the screen.

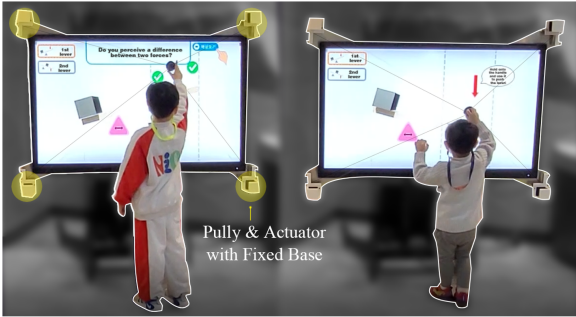


Fig. 2. An example of a haptic interface used in education context: our previous prototype of a cable driven haptic interface that can interact with existing educational content and settings. The motivation of the proposed haptic device stems from the challenges posed by limited workspace and anisotropic force feedback.

Despite the benefits of the cable-driven mechanism, inherently, the workspace is limited and the force exertion capability is anisotropic for the end-effector's position. This is because the actuator can only pull the cable and not push it to transmit the force, and particular attention needs to be paid to maintain the tension in the cable to prevent slack. Several studies in literature focused on increasing the isotropic force exertion and expanding the workspace of the cable-driven mechanism. Increasing the number of cables or pulleys expands the workspace [7], [8], [9], but cannot fully cover the rectangular screen without a remaining unreachable workspace. Recently, a counterbalancing mechanism has been proposed to expand the workspace and increase the isotropic force to the desired area [10]. While this approach is promising, it still has a part of the workspace that remains unreachable when it comes to covering a rectangular screen.

Another approach found in literature involves deploying an adaptive mechanism to control the position of the pulley or actuator [11], [12], [13], [14]. This approach offers the advantage of a lower possibility of cable interference while concurrently expanding the workspace and force exertion [13]. However, most studies focus on theoretical analysis or applications that require periodic position control only without impedance control. One study applied an adaptive mechanism to a haptic interface [14] that partially expanded the workspace with one-degree-of-freedom (1-DoF) movement of one pulley. However, the study did not provide generalized kinematic or static analyses when all of the  $n$  numbers of pulleys move in an arbitrary plane. Moreover, an experimental evaluation of a haptic interface with multiple movable bases has not been studied.

In this study, we propose a two-degree-of-freedom (2-DoF) cable-driven haptic interface, where all pulleys have an additional degree-of-freedom thanks to a movable base, as shown in Fig. 1. The proposed system maximizes the range of isotropic forces as kinesthetic feedback for the workspace without any dead zone or unreachable workspace on a commercial screen. Additionally, the bandwidth, Z-width, perceptual performance and usability are experimentally evaluated to demonstrate the feasibility as a haptic interface with movable pulleys.

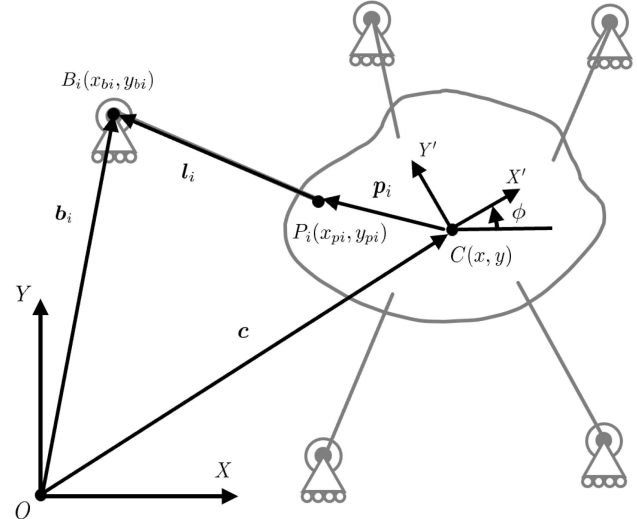


Fig. 3. Kinematic diagram for planar, cable-driven mechanism with  $n$  cables and movable pulleys.

The remainder of this article is structured as follows. In Section II, the kinematic and static analyses of the planar cable-driven mechanism with movable pulleys are introduced. In Section III, a prototype of a planar cable-driven haptic interface with movable bases is designed. In Section IV, the characterizations as a haptic interface are experimentally evaluated for the prototype. Finally, Section V concludes the article with a discussion of the results and future works.

## II. ANALYSIS OF THE PLANAR CABLE-DRIVEN HAPTIC INTERFACE WITH MOVABLE PULLEYS

This section presents the generalized kinematics and statics of a planar cable-driven haptic interface with  $n$  cables and movable pulleys.

### A. Kinematic Analysis

Kinematic analysis provides the position and velocity relationships between the pulleys/actuators (joint space) and a rigid body end-effector (task space). Unlike the linkage-driven bar mechanism, the cable-driven mechanism involves cables with varying lengths. Previous studies have explored the kinematic analysis of the parallel cable-driven mechanism, but they did not account for movable pulleys [15] or conducted analysis for a general number of cables [16].

Fig. 3 illustrates a kinematic diagram for the planar cable-driven mechanism with  $n$  number of cables and movable base-pulleys.  $O - XY$  is a fixed global coordinate and  $C - X'Y'$  is a movable reference frame fixed on the end-effector. Note that the fixed global coordinate frame  $O - XY$  is used throughout the following analysis. Based on the diagram, cable vector  $l_i$  can be expressed with base position vector  $b_i$ , end-effector's center-of-mass location  $c$ , rotation matrix  $R$  and cable attachment point vector

$p_i$ .

$$\mathbf{l}_i = \mathbf{b}_i - \mathbf{c} - \mathbf{R}\mathbf{p}_i \in \mathbb{R}^{2 \times 1} \quad (i = 1, \dots, n) \quad (1)$$

By taking  $L_2$  norm, differentiating with respect to time, and dividing by two its equation which expresses cable vector, a velocity relationship can be established as follows [15], [16].

$$\begin{aligned} l_i \dot{l}_i &= \mathbf{c}^T \dot{\mathbf{c}} + (\mathbf{R}\mathbf{p}_i)^T \dot{\mathbf{c}} + \mathbf{c}^T \dot{\mathbf{R}}\mathbf{p}_i - \mathbf{b}_i^T \dot{\mathbf{c}} \\ &\quad - \mathbf{c}^T \dot{\mathbf{b}}_i - (\mathbf{R}\mathbf{p}_i)^T \dot{\mathbf{b}}_i + \mathbf{b}_i^T \dot{\mathbf{b}}_i - \mathbf{b}_i^T \dot{\mathbf{R}}\mathbf{p}_i \quad (2) \\ \text{where } \dot{\mathbf{R}} &= \dot{\phi} \mathbf{E} \mathbf{R}, \quad \mathbf{E} = \begin{bmatrix} 0 & -1 \\ 1 & 0 \end{bmatrix} \end{aligned}$$

It is worth noting that  $\dot{\mathbf{p}}_i = 0$  for all  $i$  because  $\mathbf{p}$  has been fixed. By separating the joint-space- and task-space-related vectors, (2) is expressed as

$$l_i \dot{l}_i - \mathbf{l}_i^T \dot{\mathbf{b}}_i = -\mathbf{l}_i^T \dot{\mathbf{c}} + (\mathbf{c} - \mathbf{b}_i)^T \mathbf{E} \mathbf{R} \mathbf{p}_i \dot{\phi} \quad (3)$$

This velocity equation can be expressed as

$$\mathbf{A} \dot{\mathbf{q}} = \mathbf{B} \dot{\mathbf{x}} \quad (4)$$

where

$$\begin{aligned} \dot{\mathbf{q}} &= \left[ \dot{l}_1 \quad x_{b1} \quad y_{b1} \quad \cdots \quad \dot{l}_n \quad x_{bn} \quad y_{bn} \right]^T \in \mathbb{R}^{3n \times 1}, \\ \dot{\mathbf{x}} &= \left[ \dot{x} \quad \dot{y} \quad \dot{\phi} \right] \in \mathbb{R}^{3 \times 1}, \\ \mathbf{A} &= \begin{bmatrix} l_1 & -l_{1x} & -l_{1y} & 0 & 0 & 0 \\ & & & \ddots & & \\ 0 & 0 & 0 & l_n & -l_{nx} & -l_{ny} \end{bmatrix} \in \mathbb{R}^{n \times 3n}, \\ \mathbf{B} &= \begin{bmatrix} -l_{1x} & -l_{1y} & (\mathbf{c} - \mathbf{b}_1)^T \mathbf{E} \mathbf{R} \mathbf{p}_1 \\ \vdots & & \\ -l_{nx} & -l_{ny} & (\mathbf{c} - \mathbf{b}_n)^T \mathbf{E} \mathbf{R} \mathbf{p}_n \end{bmatrix} \in \mathbb{R}^{n \times 3} \quad (5) \end{aligned}$$

$\dot{\mathbf{q}}$  represents the velocity with respect to the cables and bases, while  $\dot{\mathbf{x}}$  represents the velocity with respect to the end-effector. It should be noted that  $\dot{\mathbf{q}}$  is in the joint space, whereas  $\dot{\mathbf{x}}$  is in the task space. The components  $x_{bi}$  and  $y_{bi}$  correspond to the  $x$ - and  $y$ -directional velocities of the  $i$ th movable base  $\mathbf{b}_i$ , respectively. Additionally,  $l_{ix}$  and  $l_{iy}$  represent the  $x$ - and  $y$ -directional components of the  $i$ th cable vector  $\mathbf{l}_i$ , respectively.

By assuming that  $\mathbf{A}$  and  $\mathbf{B}$  are full rank, the velocity relationship between the joint and task spaces can be defined by the Jacobian matrix  $\mathbf{J}$

$$\dot{\mathbf{x}} = \mathbf{B}^+ \mathbf{A} \dot{\mathbf{q}} = \mathbf{J} \dot{\mathbf{q}} \quad (6)$$

where  $\mathbf{B}^+$  represents the pseudo inverse matrix of  $\mathbf{B}$  and  $\mathbf{J} \in \mathbb{R}^{3 \times 3n}$ .

Additionally, forward kinematics calculates the position and orientation of the end-effector. The iterative Newton-Raphson method is one approach used for this purpose [16], [17]. Numerical forward kinematics can be performed using an iterative algorithm.

### B. Static Analysis

A cable-driven haptic interface generates desired force or moment on the end-effector by adjusting cable tensions. Therefore, we can formulate the static relationship between cable tension and the resulting wrench on the end-effector as follows.

$$\mathbf{ST} = \mathbf{W} \quad (7)$$

where

$$\mathbf{S} = \begin{bmatrix} \hat{l}_{1x} & \hat{l}_{2x} & \cdots & \hat{l}_{nx} \\ \hat{l}_{1y} & \hat{l}_{2y} & \cdots & \hat{l}_{ny} \\ \mathbf{R}\mathbf{p}_1 \times \hat{\mathbf{l}}_1 & \mathbf{R}\mathbf{p}_2 \times \hat{\mathbf{l}}_2 & \cdots & \mathbf{R}\mathbf{p}_n \times \hat{\mathbf{l}}_n \end{bmatrix} \in \mathbb{R}^{3 \times n},$$

$$\mathbf{T} = \begin{bmatrix} T_1 & T_2 & \cdots & T_n \end{bmatrix}^T \in \mathbb{R}^{n \times 1},$$

$$\mathbf{W} = \begin{bmatrix} F_x & F_y & M_z \end{bmatrix}^T \in \mathbb{R}^{3 \times 1}$$

$\mathbf{S}$  represents the static equilibrium equation matrix, accounting for force and moment equilibrium in the  $x$ -,  $y$ -, and  $z$ -directions.  $\mathbf{T}$  denotes the cable tension vector, while  $\mathbf{W}$  represents the desired wrench vector on the end-effector. The components  $\hat{l}_{ix}$  and  $\hat{l}_{iy}$  correspond to the  $x$ - and  $y$ -directions of the directional unit vector  $\hat{\mathbf{l}}_i$  associated with the  $i$ th cable at equilibrium. In systems with redundancy ( $n > 3$ ), infinite solutions exist for satisfying the static equation. It should be noted that using the pseudo inverse of the static equation matrix to calculate a solution does not guarantee positive cable tensions.

The relationship between the wrench on the end-effector and forces on the cable or movable base can be determined when the static equilibrium condition is met. This relationship corresponds to the wrench vector in the task space and the force vectors in the joint space. The following equation, derived from the virtual work principle, expresses this relationship.

$$\mathbf{F}^T \dot{\mathbf{q}} + \mathbf{W}^T \dot{\mathbf{x}} = 0 \quad (8)$$

$\mathbf{F}$  is a joint-space force vector with cable tensions and forces exerted by movable bases.  $F_{pix}$  and  $F_{pyi}$  represent the  $x$ - and  $y$ -directional forces that the  $i$ th movable base exerts, respectively.

By substituting (6) into (8), we obtain the direct relationship as

$$\mathbf{F}^T \dot{\mathbf{q}} + \mathbf{W}^T \mathbf{B}^+ \mathbf{A} \dot{\mathbf{q}} = \mathbf{F}^T \dot{\mathbf{q}} + \mathbf{W}^T \mathbf{J} \dot{\mathbf{q}} = 0 \quad (9)$$

which provides a direct relationship between the task space wrench vector and joint space force vector as follows,

$$\mathbf{F} = -\mathbf{J}^T \mathbf{W} \quad (10)$$

### III. SYSTEM DESIGN

This section introduces the definitions of workspace and isotropic force exertion. It outlines the process of maximizing the workspace and isotropic force exertion range using movable pulleys through generalized analyses. The system design, including the hardware setup, kinematic and static analyses, and control structure is described to design a prototype and experimentally validate the maximization.

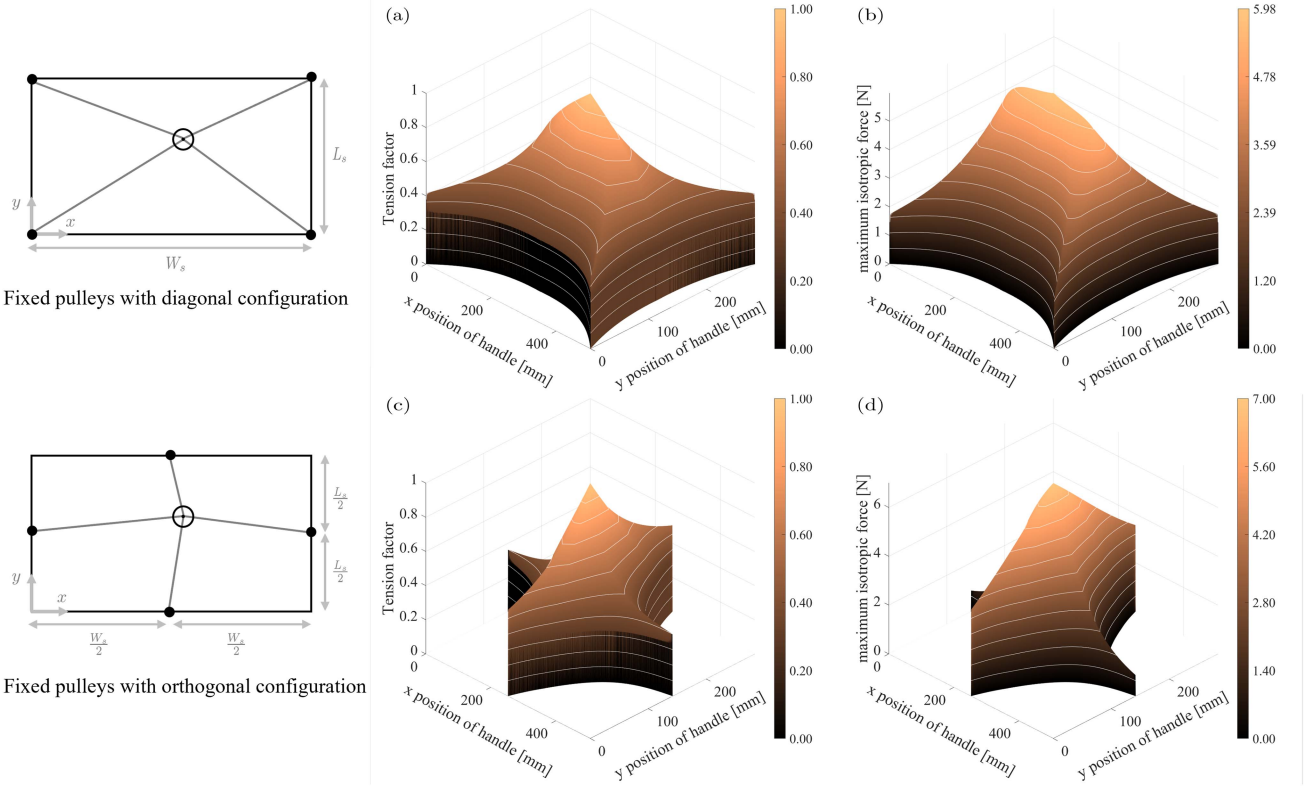


Fig. 4. Top row shows the four fixed pulleys with the diagonal configuration, with its tension factor (a) and the maximum isotropic force (b) calculation results. Bottom row shows the orthogonal configuration with its tension factor (c) and the maximum isotropic force (d) calculation results. The area without any tension factor value represents a region excluded from the wrench-feasible workspace (WFW). The values of  $W_s = 506$  mm and  $L_s = 284$  mm were set based on the size of a 23" 16:9 ratio screen display.  $T_{\min} = 3.0$  N,  $T_{\max} = 10.0$  N.

#### A. Definitions of Workspace and Isotropic Force Exertion

To define the workspace and isotropic force exertion range, we introduce the concept of the wrench-feasible workspace (WFW) [18], tension factor (TF) [19], and maximum isotropic force ( $I_F$ ) [20], [21], [22]. The WFW is determined by the geometric parameters, a specific set of wrenches, and the range of cable tensions [18].

When a given set of wrenches and end-effector pose form the WFW for a planar cable-driven mechanism, we can express its mathematical condition using the nomenclature introduced in Section II as

$$\begin{aligned} \exists(T_1, T_2, \dots, T_n) \in [T_{\min} \geq 0, T_{\max}] \\ \text{s.t. } \mathbf{S}\mathbf{T} = \mathbf{W} \in \mathbb{R}^3 \end{aligned} \quad (11)$$

It should be noted that minimum and maximum cable tension values are essential to prevent cable slack and avoid exceeding the motor torque limit in the WFW. The particular cable tension solution that satisfies the static equation and workspace criterion can be calculated. In a redundant system with  $n > 3$ , relying solely on the equation and criterion constraints leads to infinite solution. To address this, one approach is to minimize the tension magnitude using the  $L_2$  norm, reducing system energy and required torque. By incorporating this condition, a quadratic optimization problem with WFW constraints can be formulated

as

$$\begin{aligned} \min_{\mathbf{T}} \quad & \|\mathbf{T}\| \\ \text{s.t.} \quad & \mathbf{S}\mathbf{T} = \mathbf{W}, \\ & T_{\min} \leq T_i \leq T_{\max} \quad (i = 1, \dots, n, T_{\min} \geq 0) \end{aligned} \quad (12)$$

The presence of an optimal solution from (12) indicates that given pose lies within the WFW for a specified set of  $\mathbf{W}$ , as  $\mathbf{S}$  is dependent on the end-effector's pose. Conversely, if no cable tension vector satisfies (12) for any wrench, the pose falls outside the WFW.

TF is defined as the minimum tension over the maximum tension of the cables when the end-effector is in a workspace [19] as follows

$$\text{TF} = \frac{\min(\mathbf{T}^0)}{\max(\mathbf{T}^0)} \quad (13)$$

$\mathbf{T}^0$  is a homogeneous solution of (12), the optimal and nontrivial solution with a zero wrench ( $\mathbf{W} = 0$ ). It reflects the tension distribution among the cables to maintain the cable tension at a certain pose of the end-effector within the workspace. Note that  $\mathbf{T}^0$  cannot be calculated from (12) if the end-effector is out of the workspace.

TF quantifies the end-effector's pose change capability, while  $I_F$  represents the isotropic force exertion capability [11], [20],

[21], [22]. To calculate  $I_F$ , the cable tension margins are adjusted to prevent slack, and the resulting combination of tension margins forms a polygon representing the possible force magnitude and direction. The  $I_F$  value is then determined based on this polygon, considering the obtainable force magnitude in every direction. A more detailed explanation of this process will be provided in the following subsection.

### B. Optimization With Movable Pulleys

In this study, the interface focuses on generating planar force feedback using four pulleys. While three pulleys are enough for generating planar force feedback, they need to be arranged in an equilateral triangle configuration across the entire screen area to achieve isotropic force exertion [11]. This necessitates each pulley to have 2-DoF, resulting in a total of nine actuators ( $2 \times 3$  for base mobility and  $1 \times 3$  for cable actuation). In contrast, four pulleys offer the advantage of reducing the number of actuators to eight ( $1 \times 4$  for base mobility and  $1 \times 4$  for cable actuation) while still covering the target area, as demonstrated in this subsection.

Common cable-driven systems typically employ fixed pulleys to simplify system control and minimize the number of actuators. However, this approach has inevitable limitations when it comes to achieving a spacious workspace for a haptic interface. To illustrate these limitations, two configurations of four fixed pulleys, namely diagonal and orthogonal, were considered in Fig. 4. Each subfigure in Fig. 4 presents the TF and  $I_F$  analyses for the diagonal and orthogonal configurations using four fixed pulleys, with  $T_{\min} = 3.0$  N and  $T_{\max} = 10.0$  N. The tension range is determined based on the feasible motor torque (DCX26 L, Maxon, Switzerland) and the pulley diameter (10 mm) mentioned in the subsequent subsection. In terms of the WFW, the diagonal configuration exhibits a larger WFW for zero wrench compared to the orthogonal configuration, primarily around the vertices. As for  $I_F$ , both configurations yield maximum values at the center, specifically 5.98 N for the diagonal configuration and 7.00 N for the orthogonal configuration. However, regardless of the configuration, the quality of the workspace and force exertion capability degrade as the end-effector approaches the edges of the target screen area. Both configurations fall outside the WFW near the edges. Particularly, when the end-effector pose is far from the center towards the WFW boundaries,  $I_F$  and TF decrease to 0 and 0.3, respectively. It should be emphasized that 0.3 represents the lower limit for TF in the WFW within the given tension range from (13). Consequently, the fixed-base mechanism does not meet the design requirement of a large workspace without a dead zone.

The proposed system, unlike the fixed-base mechanism, incorporates movable pulleys enabling variations in the system's kinematics even with a fixed end-effector pose. This feature allows for the maximization of the workspace and isotropic force exertion range by defining a performance index as a cost function. To illustrate, the optimization problem that identifies the configuration of  $q$  maximizing the TF for a given end-effector

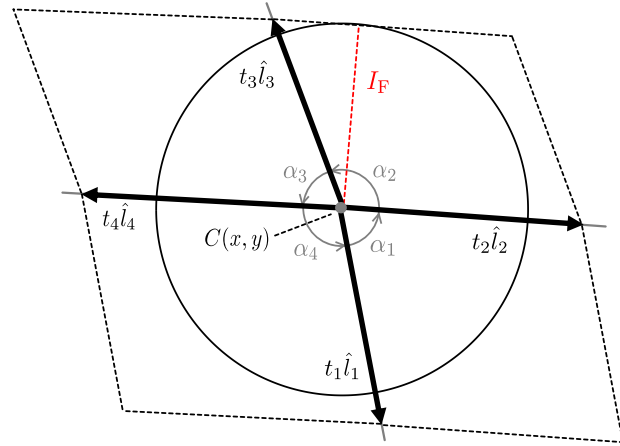


Fig. 5. Force diagram used to calculate  $I_F$  for a planar, two-degree-of-freedom, cable-driven system with four pulleys. Each parallelogram represents the magnitude and direction of the force using a combination of adjacent  $f_i \hat{l}_i$  vectors.  $I_F$  can be evaluated as the radius of the circle that is tangent to the polygon and is centered at the end-effector's mass center.

position  $x$  can be formulated as follows:

$$\begin{aligned} \max_q \quad & \text{TF} \\ \text{s.t. } & x = \text{FK}(q) \end{aligned} \quad (14)$$

and one that maximizes  $I_F$  is

$$\begin{aligned} \max_q \quad & I_F \\ \text{s.t. } & x = \text{FK}(q) \end{aligned} \quad (15)$$

where  $\text{FK}$  is a function or algorithm that executes forward kinematics.

To find the optimal solution for (14) in the case of four pulleys, it is important to note that TF represents the ratio between the minimum and maximum tensions as defined in (13). By employing a straightforward mathematical relationship, TF can be expressed as:

$$\text{TF} = \frac{\min(\mathbf{T}^0)}{\max(\mathbf{T}^0)} = \frac{\min(\mathbf{T}^0)}{\min(\mathbf{T}^0) + \Delta T} \quad (\Delta T \geq 0) \quad (16)$$

where  $\Delta T$  represents the difference between the  $\max(\mathbf{T}^0)$  and  $\min(\mathbf{T}^0)$ , where  $\mathbf{T}^0$  corresponds to the homogeneous solution of the static equation satisfying the WFW constraints. Specifically,  $\mathbf{T}^0$  is the optimal and nontrivial solution of (12) when the wrench is zero. When  $\Delta T$  is zero, the TF reaches its maximum value of one, indicating that all the elements of  $\mathbf{T}$  have the equal magnitudes. This condition is achieved only when all cables align symmetrically with respect to the end-effector position.

In (15), it is essential to consider the computation procedure for  $I_F$  as described in [11], [20]. Fig. 5 provides a graphical interpretation of the  $I_F$  calculation for the case of four pulleys. In this diagram,  $t_i$  represents the remaining tension gain on the  $i$ th cable when the end-effector pose is within the WFW under the zero-wrench condition, and  $\hat{l}_i$  denotes the directional vector along the  $i$ th cable. Hence,  $t_i \hat{l}_i = (T_{\max} - T_i^0) \hat{l}_i$ , where  $T_i^0$  corresponds to the  $i$ th element of the  $\mathbf{T}^0$ . Additionally,  $\alpha_i$  signifies the angle between the  $i$ th and  $(\text{mod}(i, 4) + 1)$ th

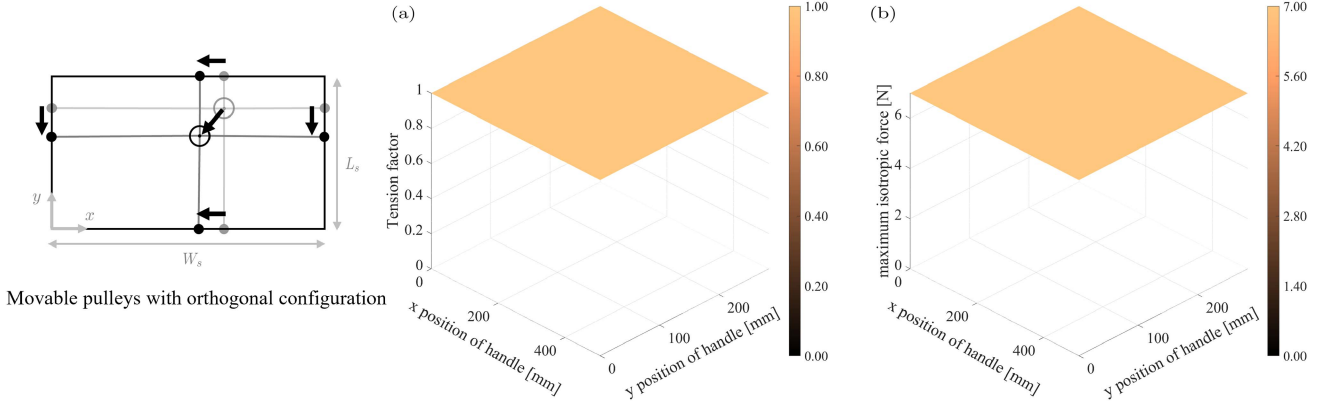


Fig. 6. Tension factor (a) and maximum isotropic force calculation (b) results for four cables and movable pulleys with orthogonal configuration.  $W_s = 506$  mm and  $L_s = 284$  mm were set based on the size of a 23" screen display.  $T_{\min} = 3.0$  N,  $T_{\max} = 10.0$  N.

cable, representing the angle between two adjacent cables in the counterclockwise rotational direction. The dotted-line polygon in the diagram consists of four parallelograms, each representing the magnitude and direction of the force using a combination of adjacent  $t_i \hat{l}_i$  vectors. The value of  $I_F$  can be determined as the radius of the circle tangent to the polygon and centered at the end-effector's center of mass. Mathematically, this can be formulated as

$$I_F = \min_{i=1,2,3,4} r_i \quad (17)$$

where

$$r_i = \begin{cases} \min (||\mathbf{u}_i||, ||\mathbf{v}_i||) & (0 < \alpha_i \leq \frac{\pi}{2}) \\ \min \left( \frac{||\mathbf{u}_i \times \mathbf{v}_i \cdot \mathbf{k}||}{||\mathbf{u}_i||}, \frac{||\mathbf{u}_i \times \mathbf{v}_i \cdot \mathbf{k}||}{||\mathbf{v}_i||} \right) & (\frac{\pi}{2} < \alpha_i \leq \pi) \end{cases}$$

in which  $\mathbf{u}_i = t_i \hat{l}_i$ ,  $\mathbf{v}_i = t_{(\text{mod}(i,4)+1)} \hat{l}_{(\text{mod}(i,4)+1)}$ ,  $\mathbf{k} = [0 \ 0 \ 1]^T$ . The value of  $r_i$  represents the maximum force magnitude that can cover any direction within a parallelogram formed by two adjacent vectors,  $t_i \hat{l}_i$  and  $t_{(\text{mod}(i,4)+1)} \hat{l}_{(\text{mod}(i,4)+1)}$ . It should be noted that the computation of  $r_i$  is influenced by  $\alpha_i$ , which cannot exceed  $\pi$  since the system is within the WFW under zero-wrench condition with four cables.

Based on (17), two requirements can be inferred to maximize  $I_F$ . Firstly, it is necessary to maximize the tension gain for each cable, resulting in minimizing the magnitude of  $T_i^0$ . This ensures a larger polygon area, as depicted in Fig. 5. Secondly, all angles between two adjacent cables should be equal or less than  $\pi/2$  ( $0 < \alpha_i \leq \pi/2$ ). When an angle is between  $\pi/2$  and  $\pi$  ( $\pi/2 < \alpha_i \leq \pi$ ),  $r_i$  is computed as the height of the parallelogram, which is smaller than the magnitudes of the vectors used in the cross product. Therefore, it is recommended to use smaller alpha to guarantee a larger  $r_i$  subject to constant tension gain. Consequently, only an orthogonal cable configuration, where all  $\alpha_i$  values are  $\pi/2$ , satisfies both conditions simultaneously. In the orthogonal configuration, all cables require only the  $T_{\min}$  tension for the system to operate within the WFW under the zero-wrench condition, fulfilling the first requirement. Furthermore, the orthogonal configuration is the only possible arrangement

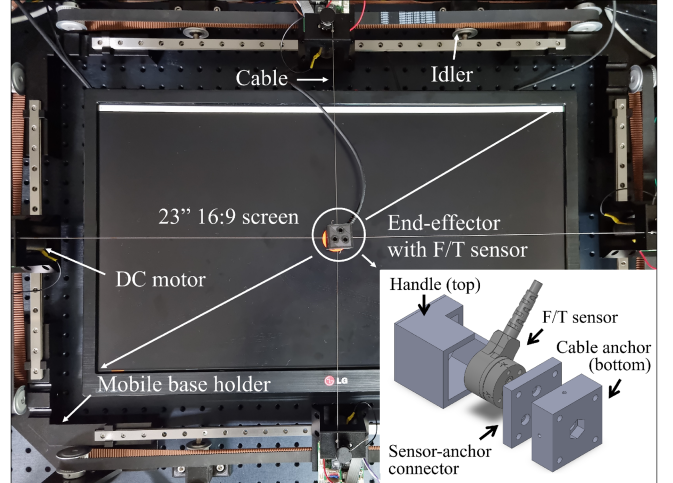


Fig. 7. Top view of the proposed system. The end-effector contains three housing parts and a F/T sensor (bottom right). The handle is where a user holds the end-effector. The sensor-anchor connector connects the sensor and cable anchor so that the F/T sensor can sense force and torque. All cables are fixed in the center of the cable anchor.

for a four-pulley system to satisfy the second condition, as the sum of the four angles should be  $2\pi$ .

The orthogonal configuration simultaneously achieves maximum TF and  $I_F$  as a subset of symmetric configurations. Selecting a configuration aligned with the task space coordinate intuitively realizes the orthogonal configuration. In this case, each base moving along the  $x$ - or  $y$ -direction shares the same  $x$  or  $y$  values as the end-effector in the global fixed frame, maintaining an orthogonal configuration. Fig. 6 illustrates the TF and IF calculation results, neglecting pulley and actuator sizes. The movable pulleys with an orthogonal configuration cover the entire screen area, except at kinematic singularities, providing maximum workspace and isotropic force exertion range. To achieve the required design parameters, the proposed interface must maintain the orthogonal configuration relative to the end-effector position. This requires a total of eight actuators, four for base mobility and four for cable actuation.

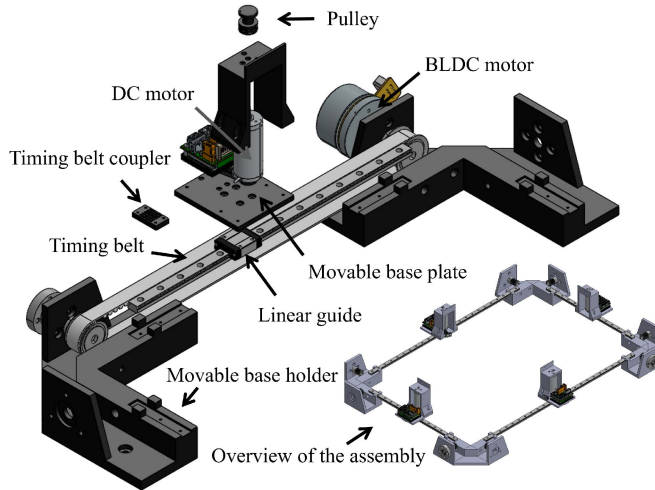


Fig. 8. Isometric view of the prototype design between the movable base and cable system for one axis (top left). The identical design was used for the four sides of the display (bottom right).

### C. Hardware Description

Figs. 1 and 7 illustrate an overview of the interface (1100 mm  $\times$  650 mm  $\times$  165 mm). The proposed interface has two parts: a *movable base* and the *cable system* to make the pulleys movable. A 23" 16:9 ratio screen display can be placed at the center of the interface.

The movable base incorporates non/geared BLDC motors (EC 60 Flat, Maxon, Switzerland) with a linear guide and timing belt mechanism to actively adjust its position. Four BLDC motors, controlled by compatible motor drivers (EPOS4 70/15, Maxon, Switzerland), provide 1-DoF movement for each movable base plate. Idlers were deployed to maintain timing belt tension and minimize variance in mechanical characteristics. The movable base holders were mechanically fixed with the motors, shaft, linear guide, and bottom aluminum plate. Additional housing on the side accommodates the motors, motor drivers, and a switched-mode power supply.

The cable system employs non/geared direct current (DC) motors (DCX26 L, Maxon, Switzerland), pulleys, and cable transmissions to generate force. Four DC motors, controlled by different motor drivers (EPOS4 Compact 24/1.5 EtherCAT, Maxon, Switzerland), reduce weight on the timing-belt mechanism of the movable base. Each motor was clamped to a base plate, providing 1-DoF movement for the pulley. Fig. 8 illustrates the assembly between the cable system and movable base. All pulleys were made of aluminum with a diameter of 10 mm. A stainless-steel cable (Bare 1 $\times$ 7, CarlStahl, Germany) with high stiffness and working cycle was selected. The end-effector features a covered six-axis force torque (F/T) sensor (Nano17-E, ATI, Canada).

Considering the recommended update rates of the haptic interface controller to be 1 kHz or higher [23], the controller's control frequency was set to 1 kHz. The control was performed in real-time using a C++ controller operating on Windows 10 (TwinCAT, Beckhoff, Germany). To ensure fast and reliable

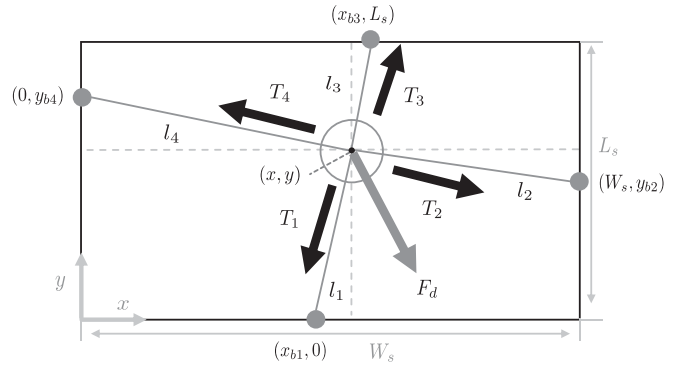


Fig. 9. Diagram of kinematic, cable tension, and end-effector's force for the proposed system.

communication, EtherCAT communication was implemented. A compatible motor driver module (581245, Maxon, Switzerland) and a DAQ (PCIe-6351, National Instruments, USA) were used for the F/T sensor.

### D. Kinematics and Statics Analyses for the Proposed System

Fig. 9 illustrates the kinematic and force diagrams of the proposed interface, depicting the positions of the end-effector denoted as  $x$  and  $y$ . To prevent mechanical rotation, all cables are connected at the center of the end-effector. Thus, the orientation of the end-effector and moment generation are not considered, resulting a zero value for  $p$  in (2) geometrically. Each cable is attached to the  $i$ th movable base, with positions defined as  $x_{bi}$  or  $y_{bi}$ . The first and third movable bases move only in the  $x$ -direction, while the second and fourth movable bases move only in the  $y$ -direction. The maximum dimensions of the coordinate frame are width ( $W_s$ ) = 711.8 mm and length ( $L_s$ ) = 461.8 mm. Using this information, the cable lengths ( $l_1, l_2, l_3$ , and  $l_4$ ) can be calculated as

$$\begin{aligned} l_1 &= \sqrt{(x - x_{b1})^2 + y^2}, & l_2 &= \sqrt{(W_s - x)^2 + (y - y_{b2})^2} \\ l_3 &= \sqrt{(x_{b3} - x)^2 + (L_s - y)^2}, & l_4 &= \sqrt{x^2 + (y_{b4} - y)^2} \end{aligned} \quad (18)$$

The relationship between the joint- and task-space vectors can be expressed as

$$\boldsymbol{x} = \text{FK}(\boldsymbol{q}) \quad (19)$$

where

$$\boldsymbol{x} = \begin{bmatrix} x & y \end{bmatrix}^T,$$

$$\boldsymbol{q} = \begin{bmatrix} l_1 & x_{b1} & l_2 & y_{b2} & l_3 & x_{b3} & l_4 & y_{b4} \end{bmatrix}^T$$

and FK is an algorithm for forward kinematics based on the Newton-Raphson method. To account for the constraint that each movable base can only move along either the  $x$ - or  $y$ -direction, the joint position vector  $\boldsymbol{q}$  is represented as  $2n \times 1$  matrix, while the task position vector  $\boldsymbol{x}$  is reduced

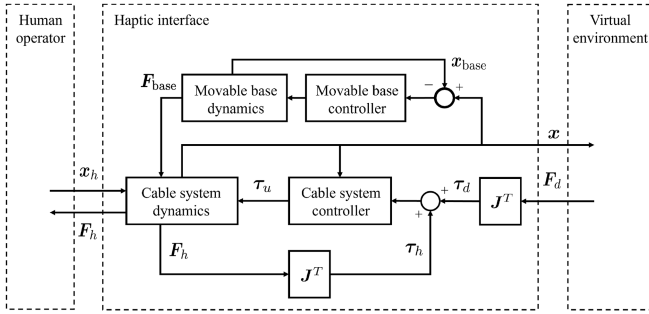


Fig. 10. Overall control structure for the proposed haptic interface, including the human operator, and virtual environment.

to a  $2 \times 1$  matrix. Herein, the Jacobian matrix can be calculated to establish the connection between joint- and task-space velocities.

$$\mathbf{J}_{(2 \times 8)} = \mathbf{B}^+ \mathbf{A} \quad (20)$$

where

$$\mathbf{A} = \begin{bmatrix} l_1 & x - x_{b1} & 0 & 0 & 0 & 0 & 0 & 0 \\ 0 & 0 & l_2 & y - y_{b2} & 0 & 0 & 0 & 0 \\ 0 & 0 & 0 & 0 & l_3 & x - x_{b3} & 0 & 0 \\ 0 & 0 & 0 & 0 & 0 & 0 & l_4 & y - y_{b4} \end{bmatrix},$$

$$\mathbf{B} = \begin{bmatrix} x - x_{b1} & y \\ x - W_s & y - y_{b2} \\ x - x_{b3} & y - L_s \\ x & y - y_{b4} \end{bmatrix}$$

Additionally, the static equilibrium equation can be established based on (7).

$$\mathbf{S}\mathbf{T} = \mathbf{F}_d \quad (21)$$

where

$$\mathbf{S} = \begin{bmatrix} -\frac{x - x_{b1}}{l_1} & \frac{W_s - x}{l_2} & \frac{x_{b3} - x}{l_3} & -\frac{x}{l_4} \\ -\frac{y}{l_1} & -\frac{y - y_{b2}}{l_2} & \frac{L_s - y}{l_3} & \frac{y_{b4} - y}{l_4} \end{bmatrix},$$

$$\mathbf{T} = [T_1 \ T_2 \ T_3 \ T_4]^T,$$

$$\mathbf{F}_d = [F_x \ F_y]^T$$

The desired wrench vector used for generating the  $\mathbf{W}$  of (7) was reduced to  $\mathbf{F}_d$ , which is a  $2 \times 1$  matrix because the interface only provides a 2-DoF force feedback on the end-effector.

### E. Control

The proposed interface incorporates movable pulleys and includes two distinct controllers. The cable system exerts force

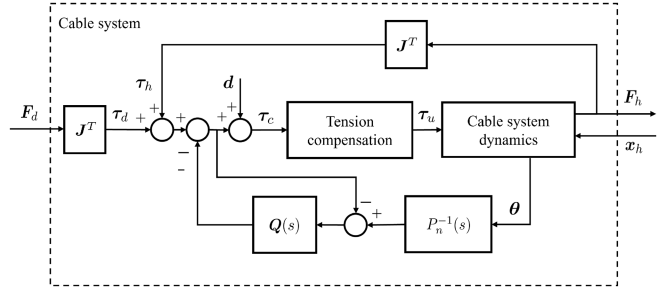


Fig. 11. Cable system controller with the disturbance-based-observer (DOB) control.

through the motor and cable transmission, while the movable base system maintains an optimal cable configuration to maximize the workspace and isotropic force exertion range. Fig. 10 illustrates the overall control structure of the proposed system. All controllers have a 1 kHz control frequency. The haptic interface can be considered as a two-port system with human operator and virtual environment, where are one-port terminations [24]. As an impedance-type haptic interface, the system interacts with a human operator by accepting the task-space position of the human hand  $x_h$  as input and providing the force perceived by humans  $F_h$  as output. Simultaneously, the system expresses the impedance of the virtual environment by receiving the desired force rendered by the virtual environment  $F_d$  and transmitting a calculated task-space position of the end-effector from the forward kinematics  $x$ . It should be noted that in the proposed system,  $x_h$ ,  $F_h$ , and  $F_d \in \mathbb{R}^2$  and  $\tau_d$ ,  $\tau_h$ , and  $\tau_u \in \mathbb{R}^4$ .

Due to the mobility of the base, a position initialization process is required for both the movable base and cable system before running each controller. A self-calibration process based on the conventional homing method is performed when the interface is enabled. The controller commands set all cable tensions of the cable system to  $T_{\min} = 3.0$  N, and each movable base moves to the edge until it is mechanically stopped. Once all movable bases have stopped, each encoder value is set as the initial position of the movable base and cable system, which are components of the joint vector  $q$ . After the position initialization process, the movable base controller maintains an orthogonal cable configuration using a proportional-integral-derivative (PID) position controller based on  $x$ , which is estimated using forward kinematics.

In the case of the cable system controller,  $\mathbf{F}_d$  is generated by exerting a corresponding torque on each motor. Fig. 11 illustrates the detailed control structure for the cable system. All cables were assumed to be rigid and massless. The controller performed quadratic programming for each cable tension to calculate the control input torque  $\tau_u$  for a given  $\mathbf{F}_d$  and maintain the minimum cable tension as follows:

$$\begin{aligned} \min_T \quad & \|T\| \\ \text{s.t.} \quad & \mathbf{S}\mathbf{T} = \mathbf{F}'_d, \\ & T_i \geq T_{\min} \quad (i = 1, \dots, 4) \end{aligned} \quad (22)$$

where

$$\mathbf{F}'_d = S\tau_c/r_p, \quad \tau_u = r_p T$$

In the algorithm, the variables were set to  $T_{\min} = 3.0 \text{ N}$  and  $r_p = 5 \text{ mm}$ .  $\mathbf{F}'_d$  is the desired effective force on the end-effector when the control input torque is applied to each motor of the cable system.  $T_{\max} = 10.0 \text{ N}$  based on the continuous motor torque range of the cable system motor. Therefore, if there are tension magnitudes that exceed  $T_{\max}$  after quadratic programming, they are set as  $T_{\max}$  as follows:

$$T_i = \begin{cases} T_{\max} & T_i > T_{\max} \\ T_i & \text{otherwise} \end{cases} \quad (23)$$

In the proposed controller, the disturbance-observer-based (DOB) control [25], [26] with a control frequency of 1 kHz is employed. The DOB controller compensates for the disturbance  $d$  affecting the motor, such as friction, to enhance system transparency, eliminating the need for additional identification process. The cable system controller as shown in Fig. 11 computes the compensation control input  $\hat{d}$  based on the desired exertion  $\mathbf{F}_d$  and external human force  $\mathbf{F}_h$ . This computation involves the utilization of the second-order binomial Q filter  $Q(s)$  and nominal motor dynamics  $P_n(s)$ , which serve as controller gains.

$$Q(s) = \frac{1}{(\tau s + 1)^2}, \quad P_n(s) = \frac{1}{J_n s^2 + B_n s} \quad (24)$$

where  $\tau$  is the filter time constant with a 5 Hz cutoff frequency,  $J_n = \text{diag}\{21, 21, 21, 21\} \text{ g} \cdot \text{cm}^2$ , and  $B_n = \text{diag}\{0.05, 0.05, 0.05, 0.05\} \text{ g} \cdot \text{m}^2/\text{s}$ . The cutoff frequency of  $\tau$  and values of  $B_n$  were set arbitrarily based on a preliminary controller tuning and  $J_n$  follows the computer-aided design data of the motor. In the proposed system,  $\hat{d}$  and  $\theta$  are  $\mathbb{R}^4$  vectors.

#### IV. PERFORMANCE EVALUATION

This section presents the experimental evaluation of the proposed haptic interface using the developed prototype. The evaluation includes quantifying the continuous force output of the system to verify the maximization of the workspace and isotropic force exertion range. Additionally, the frequency responses of the movable base, cable system, and Z-width were characterized. Finally, a user experiment was conducted to assess the overall perceptual performance and usability of the prototype.

##### A. Validation of Workspace and Isotropic Force Exertion Range Maximization

The objective of the proposed interface is to maximize the workspace and isotropic force exertion range through the implementation of pulleys. To experimentally validate this, the open-loop maximum continuous force was measured at multiple locations within the desired workspace.

The end-effector of the system was positioned at nine different locations in an orthogonal configuration. Fig. 12 illustrates the selection of eight locations near the edge of the target workspace for comparison with the conventional workspace limit, while one location around the center was chosen as a reference. To measure the output force, the F/T sensor within the end-effector

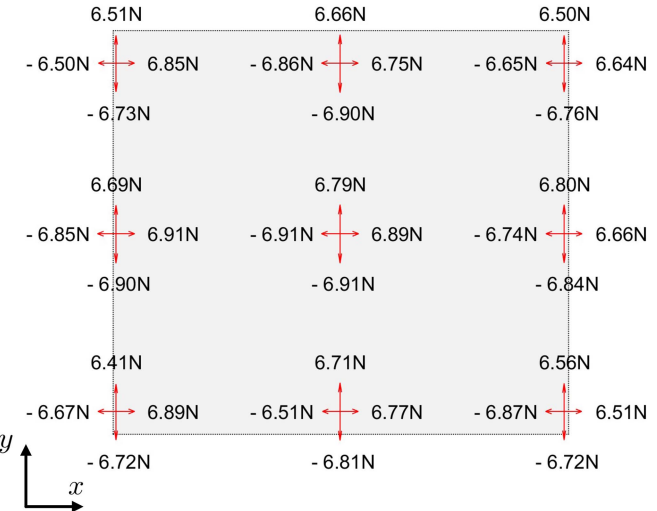


Fig. 12. Measured maximum continuous force for each direction and location. Command force magnitude is 7.0 N. The gray area represents the target workspace;  $W_s = 506 \text{ mm}$  and  $L_s = 284 \text{ mm}$  were set based on the size of a 23" 16:9 ratio screen display.

was immobilized using a beam for each location. The beam was securely attached to an aluminum plate located at the system's base. During the experiment, the controller commanded an open-loop force exertion using the following procedure: First, the force was linearly increased from zero to the target force over a period of 2 seconds. Second, the target force magnitude was maintained for 6 seconds. Finally, the target force was linearly decreased back to zero. Force data were collected at a sampling rate of 1 kHz for 6 seconds once the commanded force reached the target force. The target force was set to 7.0 N, which is equal to the difference between the minimum and maximum tension magnitudes ( $T_{\min} = 3.0 \text{ N}$ ,  $T_{\max} = 10.0 \text{ N}$ ).

The maximum continuous force was measured in four directions: the  $+x$ ,  $-x$ ,  $+y$ , and  $-y$  directions within the coordinate frame of Fig. 9<sup>1</sup> and calculated by averaging the acquired force data. Fig. 12 illustrates the maximum continuous forces for each direction and location. The maximum isotropic force for each location is calculated by selecting the minimum magnitude among the four measured maximum continuous force values. The mean measured maximum continuous force for all measuring points was 6.73 N, with a standard deviation of 0.14 N and a mean absolute error of 0.27 N, which accounts for 3.86% of the theoretical value. Regarding the maximum isotropic force, the mean value for all measuring points was 6.58 N, with a standard deviation of 0.12 N and a mean absolute error of 0.42 N, representing 6.00% of the simulated value. The theoretical maximum continuous force for each  $x$ - and  $y$ -direction, as well as the simulated maximum isotropic force, was 7.0 N. The measured magnitudes deviate from the theoretical results due to undesired disturbances such as friction, which affect the force exertion. Therefore, these results demonstrate that the movable pulleys effectively maximize the workspace and isotropic force exertion range within the target area.

<sup>1</sup>This coordinate frame is used throughout this section

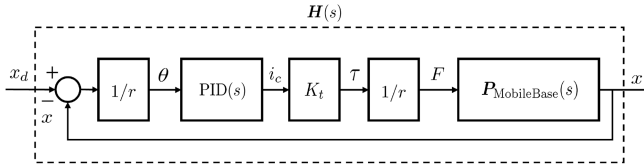


Fig. 13. Block diagram used to identify the closed-loop position frequency response of the movable base.

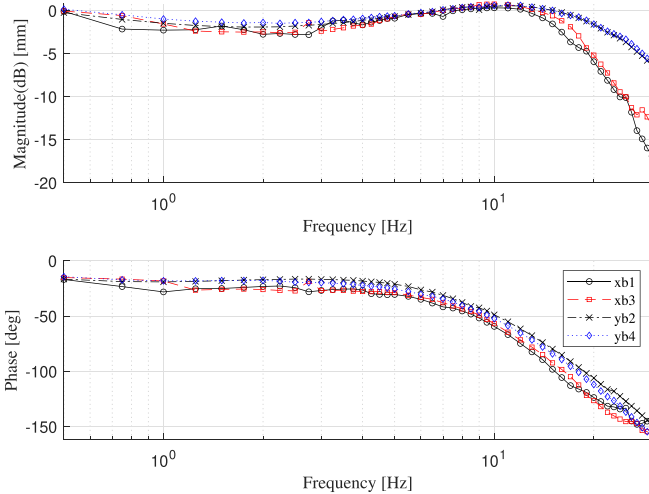


Fig. 14. Closed-loop position frequency response of each movable base using the position proportional integral derivative controller.

### B. Movable Base Characterization

The proposed system incorporates four movable bases strategically positioned to achieve an optimal cable configuration, thereby maximizing the workspace and isotropic force exertion range. It is crucial for each base to exhibit a rapid response time through the position controller in order to accurately track the end-effector's position changes. Consequently, assessing the closed-loop position frequency response of the movable bases is essential for evaluating their performance.

Fig. 13 depicts the control block diagram used to identify the closed loop position bandwidth of the movable base. The desired position  $x_d$  and the actual position  $x$  of each movable base are compared to calculate the target angle  $\theta$ , considering the timing pulley radius  $r$ . A PID position controller  $\text{PID}(s)$  is utilized to generate control output in the form of the current  $i_c$ . This current is then converted to motor torque using the motor torque constant  $K_t$ , which in turn contributes to the force  $F$  acting on the movable base dynamics. The force-position transfer function  $P_{\text{MovableBase}}(s)$  characterizes the dynamics of the movable base, while  $H(s)$  represents the closed-loop transfer function.

The frequency response of each movable base can be obtained by commanding a sine wave with a 2 mm amplitude on  $x_d$  and increasing the frequency from 0.5 to 30 Hz. The experiment was conducted with the end-effector positioned at the center of the workspace, while maintaining the initial orthogonal cable configuration of movable bases. Position data  $x_d$  and  $x$  were collected at a sampling rate of 1 kHz.

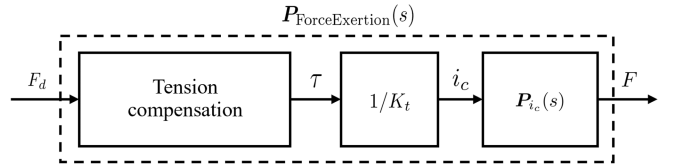


Fig. 15. Block diagram used to identify open-loop force frequency response of the system.

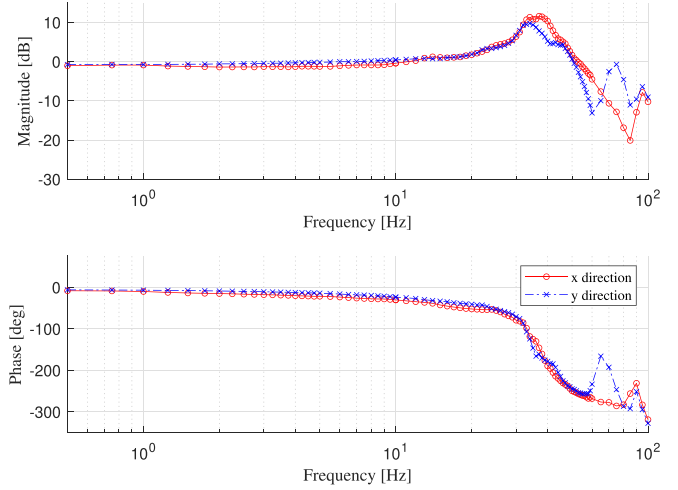


Fig. 16. Open-loop force frequency response of the cable system for each  $x$  and  $y$  direction.

Fig. 14 illustrates the Bode plots of all movable bases with respect to the position of the PID controller. It can be observed that each movable base exhibits a bandwidth of approximately 16 Hz in the  $x$ -direction and 23 Hz in the  $y$ -direction. Previous studies have indicated that humans are capable of generating maximum frequency of 4 Hz through voluntary hand movements [27], [28], [29]. Therefore, the deployed PID position controller enables the movable base to respond adequately in order to maintain an optimized configuration and track the position changes of the end-effector.

### C. Cable System Characterization

The cable system generated force feedback through the end-effector, allowing us to analyze its open-loop force exertion capability. This analysis can be performed by examining the frequency response using data from the input force command and the sensed actual force measured by a force sensor.

Fig. 15 illustrates the control block diagram for the analysis.  $F_d$  represents the desired force, while  $F$  represents the actual force generated at the end-effector. The tension compensation algorithm solves the quadratic programming problem defined in (22). The motor torque constant  $K_t$  maps the current  $i_c$  to the torque. The transfer function  $P_{i_c}(s)$  characterizes the current-force dynamics of the cable system, and  $P_{\text{ForceExertion}}(s)$  represents the open-loop transfer function for force exertion.

The force response  $F$  was evaluated by commanding a sine wave force signal  $F_d$  with a 2 N amplitude at increasing frequencies ranging from 0.5 to 100 Hz. The initial position of

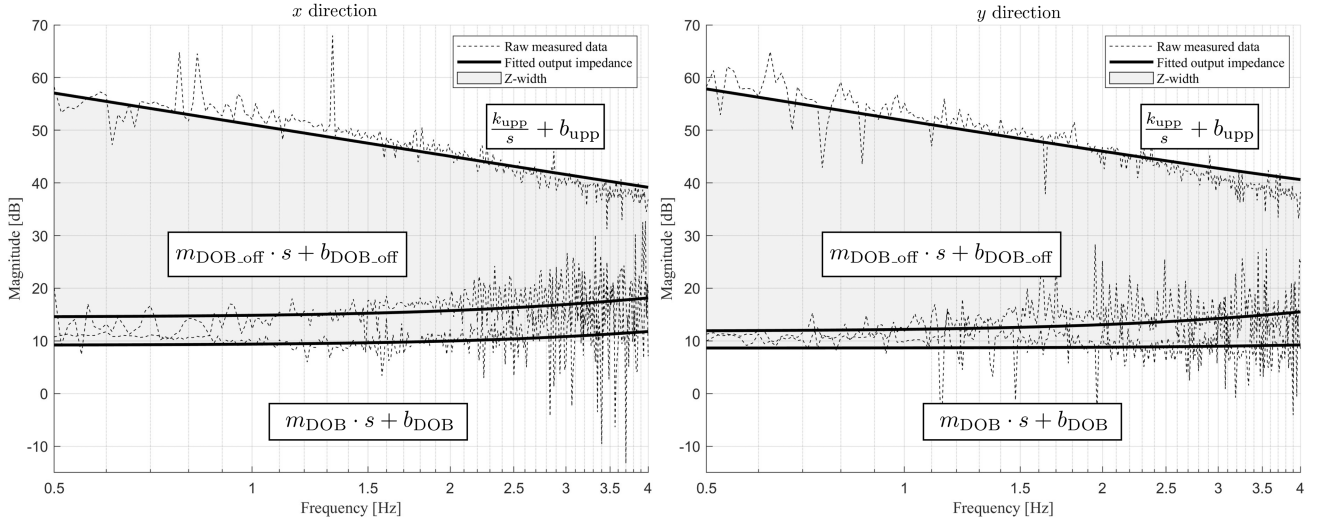


Fig. 17. Output impedances and Z-widths of the proposed interface. The two plots correspond to the  $x$  (left) and  $y$  directions (right). A spring-damper model was fitted to the impedance data with the virtual wall (top curve), and a mass-damper model was fitted to the impedance data expressing free-space (middle and bottom curve). The impedance has been plotted assuming the spring-damper model ( $k/s + b$ ) and the mass-damper model ( $ms + b$ ), each for the virtual wall and free-space data respectively, as shown in the labels.

the end-effector was at the center of the workspace, while the movable bases were positioned in the middle of their respective ranges of motion. To measure the output force  $F$ , the motion of the end-effector was constrained using a beam that was clamped to an aluminum plate beneath the system. Force data  $F_d$  and  $F$  were acquired at a sampling rate of 1 kHz.

Fig. 16 illustrates the force frequency response of the proposed interface. The plot demonstrates resonance peaks at approximately 37 Hz and 34 Hz in the  $x$ - and  $y$ -directions, respectively, accompanied by the bandwidths of approximately 58 Hz and 53 Hz in the corresponding directions. It should be noted that the resonance peaks and bandwidths may vary when the movable bases are displaced from the center. Further investigations<sup>2</sup> revealed that the bias of movable bases can modify the resonance peaks by up to 7 Hz and the bandwidths by up to 10 Hz.

#### D. Z-Width Characterization

A haptic interface generating kinesthetic force feedback can be regarded as a device that generates mechanical impedance, representing the dynamic relationship between the velocity and force [30]. By generating responsive force to the user's movement, the haptic interface can alter the dynamics of the virtual environment. This mechanical impedance is characterized by output force and velocity as

$$Z_{\text{HapticInterface}}(s) = \frac{F_{\text{output}}(s)}{v_{\text{output}}(s)} [\text{N}/(\text{m}/\text{s})] \quad (25)$$

The achievable impedance range of the interface, known as the Z-width [30], was characterized by evaluating both the

<sup>2</sup>In the experiments, the movable bases were biased in the  $-x$ ,  $+x$ ,  $-y$ , and  $+y$  directions based on the locations indicated in Fig. 12. Sine wave force signals were commanded along the  $x$ - and  $y$ -directions, with frequencies ranging from 0.5 to 100 Hz for the  $-x$  and  $+x$  biases, and  $-y$  and  $+y$  biases, respectively.

TABLE I  
Z-WIDTH, MAXIMUM AND MINIMUM IMPEDANCES

	$x$ direction	$y$ direction
Z-width (0.5 Hz / 4 Hz)	47.84 dB / 27.39 dB	49.19 dB / 31.40 dB
Maximum $k_{\text{wall}}$	3560 N/mm	3575 N/mm
Maximum $b_{\text{wall}}$	5 N/(m/s)	5 N/(m/s)
Minimum $m_{\text{free-space}}$	0.1039 kg	0.0413 kg
Minimum $b_{\text{free-space}}$	2.873 N/(m/s)	2.703 N/(m/s)

minimum and maximum impedances that the interface can generate during stable interaction with a human operator. A single participant without sensorimotor disorders performed sinusoidal perturbations in either the  $x$ - or  $y$ -direction, with the frequency continuously increasing over a period of two minutes [31]. The participant maintained the same pose for each direction to account for the variation in human hand impedance with pose [32].

The F/T sensor measured the force during the interaction, and the force and velocity data were acquired at a sampling rate of 1 kHz. For minimum impedance rendering, the cable system controller does not exert any force while the movable base controller maintains position control for movable pulleys. An experiment was conducted to compare the effects of the DOB controller on the impedance by comparing results with and without its implementation. In the case of maximum impedance rendering, a virtual wall with a simple spring-damper model was deployed in each direction. To measure the impedance in the  $x$ -direction,

$$F_x = \begin{cases} -k_{\text{wall}} \cdot (x - x_{\text{wall}}) - b_{\text{wall}} \cdot \dot{x} & \text{if } x > x_{\text{wall}} \\ 0 & \text{otherwise} \end{cases} \quad (26)$$



Fig. 18. User experiment setup with virtual wall scenario. Red dot and green rectangular on the screen represents end-effector's position and virtual wall, respectively.

and in the case of  $y$ -direction

$$F_y = \begin{cases} -k_{\text{wall}} \cdot (y - y_{\text{wall}}) - b_{\text{wall}} \cdot \dot{y} & \text{if } y > y_{\text{wall}} \\ 0 & \text{otherwise} \end{cases} \quad (27)$$

where  $F_x$  and  $F_y$  are the commanded forces in the  $x$ - and  $y$ -directions, respectively. The virtual wall parameters consist of the stiffness  $k_{\text{wall}}$  and damping  $b_{\text{wall}}$ . The positions of the end-effector are represented by  $x$  and  $y$ , while  $x_{\text{wall}}$  and  $y_{\text{wall}}$  denote the positions of the virtual wall in the  $x$ - and  $y$ -directions. The measurements were conducted using position PID control for the movable bases and DOB control for the cable system.

Fig. 17 shows the output impedance and Z-width of the proposed interface. Table I provides the Z-width, maximum stiffness and damping, and minimum mass and damping values for each direction. It should be noted that the maximum stiffness and damping values are predetermined, while the minimum mass and damping values are obtained through fitting. The frequency range considered in the evaluation spans from 0.5 Hz to 4 Hz, taking into account the voluntary frequency capabilities of the human hand motion [27], [28], [29]. Due to asymmetry between the workspace's length and width, discrepancies arise between the Z-widths and the maximum impedance in the  $x$ - and  $y$ -directions. Regarding the minimum impedance, two sets of experimental results are depicted in the figure: the middle and bottom curves represent experiments conducted with and without the DOB controller, respectively. The presence of the DOB control yields a lower impedance by effectively mitigating system disturbances.

### E. User Experiment

A human-subject experiment was conducted to explore perceptual performance and potential future applications. Six participants (four males and two females, mean age 25.0) who reported no sensorimotor abnormalities took part in the experiment. This experiment was exempted by the Institutional Review Board at the authors' institution (PIRB-2020-E050) due to the use of simple contact measuring equipment or observation equipment without resulting in physical changes. During the experiment, participants interacted with the prototype's end-effector in free space and a virtual wall, as shown in Fig. 18. The same controller setup as the  $x$ -directional virtual wall in Section

TABLE II  
QUESTIONNAIRE AND SCORE FOR THE USER EXPERIMENT

Q1. Concentration Score: 4.50 (SD = 0.55)	I could concentrate on virtual content that hits the virtual wall provided in the experiment.
Q2. Tactile Clarity Score: 4.83 (SD = 0.41)	I could feel a sufficient tactile difference between free space and the virtual wall
Q3. Lightness Score: 4.00 (SD = 0.63)	When the end-effector was moving in free space, it felt light.
Q4. Lightness Fidelity Score: 3.00 (SD = 0.63)	When the end-effector was moving in free space, I experienced a natural tactile feeling without any inconvenience.
Q5. Stiffness Fidelity Score: 4.33 (SD = 0.82)	When the end-effector hit the virtual wall, I experienced a natural tactile feeling without any inconvenience.
Q6. Convenience Score: 0.33 (SD = 0.52)	Aside from the tactile feeling, there were no inconveniences during use.

IV-D with DOB control was used. Participants continued until they felt enough exposure to the virtual environment scenario. Subsequently, they answered six questions provided in Table II using a five-point Likert scale (except for the sixth question, which required a "yes" or "no" answer) and provided additional comments explaining their answers.

Table II presents the participants' averaged responses, obtained by summing the Likert scale ratings and dividing by the number of participants. A scale of 1 or 0 was used for the sixth question's "yes" or "no" response, respectively. The table also includes the standard deviation (SD). All participants reported being able to concentrate on the virtual wall scenario (Q1) and perceive tactile difference between the virtual wall and free-space (Q2). Regarding the end-effector's perception, five participants found it to be lightweight in free-space, except for a slight heaviness during diagonal movement reported by one participant (Q3). Only one participant did not report any inconvenience related to the natural tactile feeling during free-space interaction. Regarding specific tactile experiences, five participants reported tactile differences between small and large end-effector movements, as well as a slight delayed or feeling of being stuck during planar motion (e.g., drawing a circle). They also observed unwanted tilting of the end-effector with respect to the screen display's normal direction (Q4). Five participants agreed that virtual wall interaction provided natural tactile feedback, while one participant described the wall's feeling as elastic, resembling a rubber ball rather than a hard material (Q5). Lastly, four participants reported various inconveniences with the prototype, including the absence of housing to conceal the movable base movement, high-pitched noise during movable base movement, F/T sensor cable visibility, excessive light reflection from the screen display, and the need for further hardware finishing (e.g., addressing the gap between the screen display and the movable bases) (Q6).

### V. CONCLUSION AND DISCUSSION

This article proposed a 2-DoF planar cable-driven haptic interface with movable pulleys designed for installation on smart devices and commercial screen displays. By incorporating

movable pulleys, this interface overcomes the limitations of conventional planar cable-driven mechanism with fixed pulleys, allowing for the maximization of workspace and isotropic force exertion range without any dead zones. The design and control of the proposed interface optimize the workspace and force exertion range within a targeted planar area, leveraging generalized analyses of cable-driven haptic interface with  $n$  cables and movable pulleys. Performance evaluation demonstrates that the system can deliver an average isotropic continuous force feedback of 6.58 N within the target area (when controlled to apply 7 N). The hardware setup can be adjusted to increase force based on specific requirements, such as increasing motor torque or reducing the pulley diameter. The movable base structure exhibits a sufficient controlled response to effectively track human hand motion. Additional characteristics, including force bandwidth and Z-width, are evaluated to assess haptic rendering performance. Results from the user experiment reveal opportunities for improvement in terms of perceptual and usability. Five participants noted impedance differences between vertical and horizontal axis movements or between small and large end-effector motions during free-space interaction. One participant commented on the lower stiffness of the virtual wall. Participants also reported inconveniences related to visual and auditory feedback from the movable base during prototype usage.

As the initial prototype of the planar cable-driven mechanism where all the pulleys move, several aspects of the proposed interface can be improved and optimized. For instance, the current system utilized four actuators to enable movement of all pulleys, maximizing the position response of the movable bases. However, since the target interface is a rectangular commercial screen, the number of actuators can be reduced to two by synchronizing the movements of the pulleys along the width and length directions using a suitable mechanical structure. Nevertheless, careful attention should be given to designing a mechanism that ensures synchronized movement of the two pulleys, as it may affect the position response of the movable bases. Moreover, further optimization of hardware can be explored to reduce the overall width and length of the system. One possibility is to position the movable base structure beneath the screen while keeping the pulleys above it, minimizing wasted dimensions in practical applications. Additionally, to address the issue of the F/T sensor obstructing the screen view due to its cable, as observed in the user experiment, torque sensors will be deployed on the motor joint to enhance screen visibility. Lastly, a method to restrict rotation or translation along the normal axis to the plane will be implemented by modifying the housing of the end-effector's or adding mechanical components.

In addition, the haptic feedback and usability will be improved based on the results of the user experiment. Inconsistent or delayed tactile perception during free-space interaction and high-frequency noise, which may be caused by quick prototyping of the system, can be addressed through mechanical and controller improvements. Possible solutions include optimizing the structure and weight of movable bases, enhancing the pulley's winding mechanism to maintain cable tension mechanically, fine-tuning controller gains, or deploying a different controller

structure. For the response of low stiffness in virtual wall interactions, switching to tungsten cable can resolve the issue due to its higher stiffness compared to steel cable. Lastly, visual interruptions caused by the movement of movable bases can be mitigated by adding an additional housing cover to the system. Further investigations will be conducted to verify the improvements, including assessing the perceptual quality of haptic feedback and usability factors such as movement precision, physical demand, and learning curve.

After making these improvements, experimental measurements of the educational effect of virtual content with haptic interaction will be conducted. Candidates for educational content could include physics concepts related to force and movement, such as the principle of levers, the impact of pulleys on work, interactions between electric charges, magnetic forces between magnets, chemical bonding, and gravitational forces on celestial bodies in astrophysics. The effectiveness of learning will be assessed based on the recall, inference, or transfer of target physics knowledge.

## REFERENCES

- [1] R. Crandall and E. Karadoğan, "Designing pedagogically effective haptic systems for learning: A review," *Appl. Sci.*, vol. 11, no. 14, 2021, Art. no. 6245.
- [2] I. Han and J. B. Black, "Incorporating haptic feedback in simulation for learning physics," *Comput. Educ.*, vol. 57, no. 4, pp. 2281–2290, 2011.
- [3] A. Skulmowski, S. Pradel, T. Kühnert, G. Brunnett, and G. D. Rey, "Embodied learning using a tangible user interface: The effects of haptic perception and selective pointing on a spatial learning task," *Comput. Educ.*, vol. 92, pp. 64–75, 2016.
- [4] B. Hightower, S. Lovato, J. Davison, E. Wartella, and A. M. Piper, "Haptic explorers: Supporting science journaling through mobile haptic feedback displays," *Int. J. Hum.-Comput. Stud.*, vol. 122, pp. 103–112, 2019.
- [5] R. L. Williams, M.-Y. Chen, and J. M. Seaton, "Haptics-augmented simple-machine educational tools," *J. Sci. Educ. Technol.*, vol. 12, pp. 1–12, 2003.
- [6] A. Adilkhanov, M. Rubagotti, and Z. Kappassov, "Haptic devices: Wearability-based taxonomy and literature review," *IEEE Access*, vol. 10, pp. 91923–91947, 2022.
- [7] A. Ghasemi, M. Eghtesad, and M. Farid, "Workspace analysis for planar and spatial redundant cable robots," *J. Mechanisms Robot.*, vol. 1, no. 4, 2009, Art. no. 044502.
- [8] D. McColl and L. Notash, "Workspace formulation of planar wire-actuated parallel manipulators," *Robotica*, vol. 29, no. 4, 2011, Art. no. 607.
- [9] H. Khakpour, L. Birglen, and S.-A. Tahani, "Synthesis of differentially driven planar cable parallel manipulators," *IEEE Trans. Robot.*, vol. 30, no. 3, pp. 619–630, Jun. 2014.
- [10] H. Jamshidifar, A. Khajepour, and A. H. Korayem, "Wrench feasibility and workspace expansion of planar cable-driven parallel robots by a novel passive counterbalancing mechanism," *IEEE Trans. Robot.*, vol. 37, no. 3, pp. 935–947, Jun. 2021.
- [11] G. Rosati, D. Zanotto, and S. K. Agrawal, "On the design of adaptive cable-driven systems," *J. Mechanisms Robot.*, vol. 3, no. 2, 2011.
- [12] M. Anson, A. Alamdari, and V. Krovi, "Orientation workspace and stiffness optimization of cable-driven parallel manipulators with base mobility," *J. Mechanisms Robot.*, vol. 9, no. 3, 2017, Art. no. 031011.
- [13] D. Zanotto, G. Rosati, S. Minto, and A. Rossi, "Sophia-3: A semiadaptive cable-driven rehabilitation device with a tilting working plane," *IEEE Trans. Robot.*, vol. 30, no. 4, pp. 974–979, Aug. 2014.
- [14] B. Poitrimol and H. Igarashi, "Haptic rendering and manipulability of cable-based planar haptic interface," in *Proc. JSME Annu. Conf. Robot. Mechatron.*, 2020, pp. 1P1-N01.
- [15] C. Gosselin, R. Poulin, and D. Laurendeau, "A planar parallel 3-DOF cable-driven haptic interface," in *Proc. 12th World Multi-Conf. Systemics, Cybern. Inform.*, 2008, pp. 266–271.
- [16] M. Anson, "Cable-driven parallel manipulators with base mobility: A planar case study," Ph.D. dissertation, State Univ. New York at Buffalo, Buffalo, NY, USA, 2015.

- [17] R. L. Williams II, "Cable-suspended haptic interface," *Int. J. Virtual Reality*, vol. 3, no. 3, pp. 13–20, 1998.
- [18] P. Bosscher, A. T. Riechel, and I. Ebert-Uphoff, "Wrench-feasible workspace generation for cable-driven robots," *IEEE Trans. Robot.*, vol. 22, no. 5, pp. 890–902, Oct. 2006.
- [19] C. B. Pham, S. H. Yeo, G. Yang, and I.-M. Chen, "Workspace analysis of fully restrained cable-driven manipulators," *Robot. Auton. Syst.*, vol. 57, no. 9, pp. 901–912, 2009.
- [20] P. Gallina, G. Rosati, and A. Rossi, "3-DOF wire driven planar haptic interface," *J. Intell. Robotic Syst.*, vol. 32, no. 1, pp. 23–36, 2001.
- [21] G. Rosati, D. Zanotto, and A. Rossi, "Performance assessment of a 3D cable-driven haptic device," *ASME Int. Mech. Eng. Congr. Expo.*, vol. 48739, 2008, pp. 597–606.
- [22] D. Zanotto, G. Rosati, and A. Rossi, "Performance analysis of planar cable-based parallel manipulators," in *Eng. Syst. Des. Anal.*, 2010, pp. 789–798.
- [23] V. Hayward, O. R. Astley, M. Cruz-Hernandez, D. Grant, and G. Robles-De-La-Torre, "Haptic interfaces and devices," in *Sensor Rev.*, vol. 24, pp. 16–29, 2004.
- [24] R. J. Adams and B. Hannaford, "Stable haptic interaction with virtual environments," *IEEE Trans. Robot. Automat.*, vol. 15, no. 3, pp. 465–474, Jun. 1999.
- [25] W.-H. Chen, J. Yang, L. Guo, and S. Li, "Disturbance-observer-based control and related methods—an overview," *IEEE Trans. Ind. Electron.*, vol. 63, no. 2, pp. 1083–1095, Feb. 2016.
- [26] M. J. Kim and W. K. Chung, "Disturbance-observer-based PD control of flexible joint robots for asymptotic convergence," *IEEE Trans. Robot.*, vol. 31, no. 6, pp. 1508–1516, Dec. 2015.
- [27] A. Leist, H.-J. Freund, and B. Cohen, "Comparative characteristics of predictive eye-hand tracking," *Hum. Neurobiol.*, vol. 6, pp. 19–26, 1987.
- [28] P. Neilson, "Speed of response or bandwidth of voluntary system controlling elbow position in intact man," *Med. Biol. Eng.*, vol. 10, no. 4, pp. 450–459, 1972.
- [29] E. Samur, *Performance Metrics for Haptic Interfaces*. Berlin, Germany: Springer, 2012.
- [30] J. E. Colgate and J. M. Brown, "Factors affecting the z-width of a haptic display," in *Proc. IEEE Int. Conf. Robot. Automat.*, 1994, pp. 3205–3210.
- [31] B. Vigaru, J. Sulzer, and R. Gassert, "Design and evaluation of a cable-driven fMRI-compatible haptic interface to investigate precision grip control," *IEEE Trans. Haptics*, vol. 9, no. 1, pp. 20–32, Jan.–Mar. 2016.
- [32] T. Tsuji, P. G. Morasso, K. Goto, and K. Ito, "Human hand impedance characteristics during maintained posture," *Biol. Cybern.*, vol. 72, no. 6, pp. 475–485, 1995.



**Jinhyuk Yoon** received the B.S. and M.S. degrees in mechanical engineering from the Pohang University of Science and Technology, Pohang, South Korea, in 2020 and 2022, respectively. He is currently a Robotics Software Engineer with the LivsMed, Seongnam, South Korea.



**Donghyeon Lee** received the B.S., M.S., and Ph.D. degrees in mechanical engineering from the Pohang University of Science and Technology, Pohang, South Korea, in 2016, 2018, and 2023, respectively. He is currently a Leader of R&D Team, Celloid Ltd., Pohang. His research interests include interaction control and safe robot motion for robotic manipulators.



**Junyong Bang** received the B.S. and M.S. degrees in mechanical engineering from the Pohang University of Science and Technology, Pohang, South Korea, in 2021 and 2023, respectively. He is currently a Member of R&D Team, Celloid Ltd., Pohang.



**Hyung Gon Shin** received the B.S. and Ph.D. degrees in mechanical engineering from the Pohang University of Science and Technology, Pohang, South Korea, in 2015 and 2022, respectively. He is currently a Postdoctoral Researcher with the Pohang University of Science and Technology. His research interests include medical robots and soft robots.



**Wan Kyun Chung** (Fellow, IEEE) received the B.S. degree in mechanical design from Seoul National University, Seoul, South Korea, in 1981, the M.S. degree in mechanical engineering, and the Ph.D. degree in production engineering from the Korea Advanced Institute of Science and Technology, Daejeon, South Korea, in 1983 and 1987, respectively. He is currently a Professor of mechanical engineering with the Pohang University of Science and Technology (he joined the faculty in 1987), Pohang, South Korea. In 1988, he was a Visiting Professor with the Robotics Institute at Carnegie Mellon University, Pittsburgh, PA, USA. In 1995, he was a Visiting Scholar with the University of California Berkeley, Berkeley, CA, USA. His research interests include the development of robust controllers for precision motion control, biomedical robotics, and underwater robots. He was the Senior Editor of *IEEE TRANSACTIONS ON ROBOTICS*, and the Editor-in-Chief of the *Journal of Intelligent Service Robotics*.



**Seungmoon Choi** (Senior Member, IEEE) received the B.S. and M.S. degree in control and instrumentation engineering from the Seoul National University in 1995 and 1997, respectively, and the Ph.D. degree in electrical and computer engineering from Purdue University, West Lafayette, IN, USA, in 2003. He is currently a Professor of Computer Science and Engineering with the Pohang University of Science and Technology, Pohang, South Korea. His general research interests include haptic rendering and perception with application to robotics, human-computer interaction, virtual reality, and consumer products. He was the recipient of the 2011 Early Career Award from the IEEE Technical Committee on Haptics. Since 2020, he has been an Associate Editor-in-Chief of *IEEE TRANSACTIONS ON HAPTICS*. He was the General Co-Chair of the IEEE Haptics Symposium in 2014 and 2016.



**Keehoon Kim** (Member, IEEE) received the B.S., M.S., and Ph.D. degrees in mechanical engineering from the Pohang University of Science and Technology, Pohang, South Korea, in 1999, 2001, and 2006, respectively. From 2003 to 2004, he was a Visiting Student with the Case Western Reserve University, Cleveland, OH, USA. From 2006 to 2009, he was a Postdoctoral Researcher with the Department of Mechanical Engineering, Northwestern University. He was a Senior Research Scientist from 2009 to 2015 and a Principal Research Scientist from 2015 to 2019 with the Korea Institute of Science and Technology. From 2018 to 2019, he was a Visiting Professor with the Mechanical Engineering Department, The University of Texas at Austin, Austin, TX, USA. Since 2019, he has been an Associate Professor with the Pohang University of Science and Technology. His research interests include robotics in biomedical applications, including rehabilitation robotics, surgical robotics, power assistant robotics, and bionics-haptic interfaces, and teleoperation. From 2015 to 2018, he was the Editor of the IEEE/RSJ International Conference on Intelligent Robots and Systems. Since 2016, he has been serving the IEEE RAS Technical Committee of Telerobotics as a Co-chair.